

www.acsaem.org Article

Lewis Acid—Lewis Base Interactions Promote Fast Interfacial Electron Transfers with a Pyridine-Based Donor Dye in Dye-Sensitized Solar Cells

Dinesh Nugegoda,[†] Leigh Anna Hunt,[†] Anthony Devdass, Hammad Cheema, Ryan C. Fortenberry, Jonah W. Jurss,* Nathan I. Hammer,* and Jared H. Delcamp*



Cite This: ACS Appl. Energy Mater. 2022, 5, 1516–1527



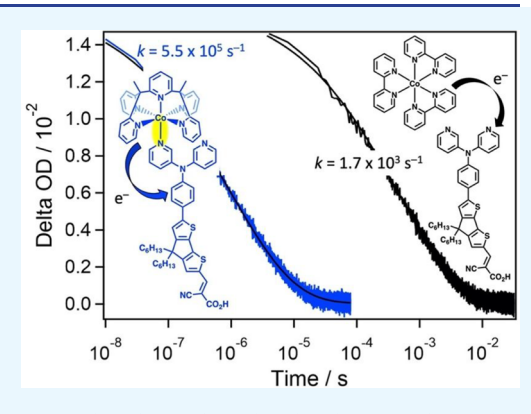
ACCESS

Metrics & More

Article Recommendations

s Supporting Information

ABSTRACT: Increasing the rate of productive interfacial electron transfer reactions in dye-sensitized solar cells is critically important toward improving device performances. Preorganized electron transfer systems at a metal oxide interface are an interesting approach toward favoring fast electron transfer reactions. This study focuses on facilitating electron transfer reactions from a redox shuttle to an oxidized dye at a TiO₂ surface via a transient redox shuttle—dye coordination complex. By design, the cobalt redox shuttle is supported by a pentadentate polypyridyl ligand with a remaining labile coordination site on the metal. The organic dye is designed with pyridyl groups on the donor region for coordinating to the open site on the redox shuttle to preorganize the redox shuttle—dye pair via a Lewis acid—Lewis base interaction. DSC devices fabricated with this dye—redox shuttle pair are studied via current—voltage curves, incident photon-to-current conversion efficiencies (IPCEs), photocurrent dynamics,



electrochemical impedance spectroscopy, and transient absorption spectroscopy. Results show that dye binding to the redox shuttle increases the rate of dye regeneration, even in the complex electrolyte environment where coordinating species such as *tert*-butylpyridine and multiple oxidation states of the redox shuttle are present, leading to a dramatically higher performance of the DSC device under fluorescent lighting $(13.0\% \text{ for } [\text{Co}(\text{PY5Me}_2)(\text{MeCN})]^{3+/2+} \text{ versus } 5.6\% \text{ PCE for } [\text{Co}(\text{bpy})_3]^{3+/2+}).$

KEYWORDS: dye-sensitized solar cells, transient absorption spectroscopy, photoinduced electron transfer, cobalt redox shuttle, Lewis acid—Lewis base interactions

■ INTRODUCTION

Dye-sensitized solar cells (DSCs) are a relatively low-cost photovoltaic technology with exception performances in practical low-light settings. $^{1-5}$ These low-light tailored devices are attractive for building integrated photovoltaics 6-10 and for use as indoor photovoltaics, which are needed to self-power Internet of Things devices. 11-13 DSCs operate with a series of electron transfer events by: (1) photoexcitation of the sensitizer and injection of an electron into TiO2, (2) electron transfer from a redox shuttle (RS) to the oxidized dye, and (3) collection of electrons from a counter electrode by the oxidized RS. 14 Increasing the rate of these productive pathways is an attractive approach toward avoiding performance losses due to competitive back electron transfer pathways. 15 Methods to increase the rate of electron transfer reaction from the RS to the oxidized dye (referred to as "regeneration") are needed to improve the overall performance of DSC devices. Typical approaches rely on diffusion-controlled regeneration; however, transiently bonded self-assembled systems through approaches such as halogen bonding have shown dramatic improvements to regeneration rates with enhanced DSC device performances. $^{16-19}$ This work seeks to probe the effects of weak Lewis acid–Lewis base (LA–LB) interactions between a TiO₂-anchored dye with a Lewis basic functionality and a Lewis acidic transition metal RS (Figure 1).

The **DN1** dye design incorporates amine-substituted pyridine rings on a triarylamine donor group with a cyclopentadithiophene (CPDT) bridge and cyanoacrylic acid (CAA) acceptor. The dye follows the high-performing donor- π bridge-acceptor (D- π -A) organic dye design, which is known to promote facile electron transfers with significant interfacial charge separation times. ²¹⁻²⁴ After photoexcitation, the D- π -A design relies on an intramolecular charge transfer (ICT) event leaving a hole on the donor region of the dye. **DN1** is designed with the Lewis basic

Received: September 18, 2021 Accepted: January 19, 2022 Published: February 4, 2022





Figure 1. LA-LB interaction between a TiO_2 -bound organic dye (DN1) and the $Co(PY5Me_2)$ redox shuttle (left). Dye (A1)²⁰ and RS (Co(bpy)₃) as control materials with no LA-LB interaction (right).

Scheme 1. Synthetic Route to DN1

pyridine groups on the donor region to hold a redox shuttle in close proximity to the photogenerated hole to promote rapid regeneration. The pyridyl groups are substituted at the 3-position to avoid weakening of the ICT event from the amine donor to the CAA acceptor. The CPDT bridge was chosen, since it has two surface protecting alkyl chains and has shown exceptional performance with transition-metal-based RSs in the literature. The CAA acceptor is known to promote facile electron injection into ${\rm TiO_2}$. We note that pyridyl groups are known to bind ${\rm TiO_2}$; however, it is anticipated that the bidentate binding carboxylic acid group is a better binding group. Likewise, the $\left[{\rm Co(PYSMe_2)(L)}\right]^{3+/2+}$ RS has been shown to be an effective RS for DSCs with organic dyes. The

prior report demonstrates the tunability of this RS with added Lewis bases such as 4-tert-butylpyridine (TBP) and methyl benzimidazole in the electrolyte, which indicate that the RS readily accepts a monodentate imine ligand (L) under operational device conditions. We hypothesize that pyridyl groups on a dye could serve as the monodentate ligand, L, in $[\text{Co}(\text{PYSMe}_2)(\text{L})]^{3+/2+}$, resulting in enhanced electron transfer reaction rates at the TiO_2 -dye-electrolyte interface. Note that throughout this manuscript, (L) is used when the ligand associated to $[\text{Co}(\text{PYSMe}_2)]^{3+/2+}$ is undefined, whereas $[\text{Co}(\text{PYSMe}_2)(\text{MeCN})]^{3+/2+}$ is written for the complex as synthesized when it is either added to an experiment or when L is known to be MeCN.

RESULTS AND DISCUSSION

The synthesis of **DN1** begins with the bromination of known *N*-phenyl-*N*-(pyridin-3-yl)pyridin-3-amine (1)²⁷ with *N*-bromosuccinimide in THF to give brominated dipyridylarylamine (2) in 64% yield (Scheme 1). Known stannylated CPDT (3)²⁸ was coupled to **2** via a Stille coupling in 81% yield to give CPDT-amine intermediate **4**. A Vilsmeier—Haack reaction at the CPDT site of **4** gives the formylated intermediate **5** in 44% yield. Finally, a Knoevenagel reaction on aldehyde **5** affords **DN1** in 84% yield in four steps from known materials in 19% overall yield.

The optical properties of **DN1** were analyzed with steady-state absorption spectroscopy. **DN1** exhibits a broad absorption band from approximately 400 to 600 nm in dichloromethane solution, which is assigned as an ICT band. A maximum absorption (λ_{max}) is observed at 515 nm with a molar absorptivity (ε) of 17 500 M⁻¹ cm⁻¹ (Figure 2). When

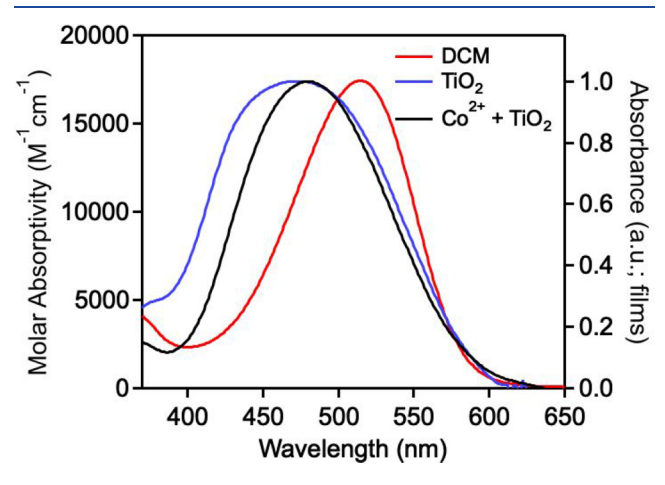


Figure 2. UV—vis absorption spectra of **DN1** in DCM, on TiO_2 , and on TiO_2 after $[Co(PY5Me_2)(MeCN)]^{2+}$ is added to the solution. The curve measured in DCM is plotted in molar absorptivity on the primary y-axis. The two curves measured on films are plotted on the secondary y-axis and normalized to the DCM peak height.

the dye is adsorbed onto TiO2, the dye absorbance has a near identical onset value with a broadening of the absorption band relative to solution measurements (Figure 2). Notably, the absorption maxima blue-shifts on TiO2 films as is commonly observed in the literature with ICT-based dyes.²⁹ In the presence of the RS, a near identical onset value is obtained with narrowing of the low-energy absorbance band with respect to dye absorbed to TiO₂. The narrowing of the absorption curve upon addition of the RS could be due to an RS-dye interaction (consistent with an LA-LB interaction) taking place at the TiO₂-dye-electrolyte interface resulting in less conformational freedom of the dye with the bulky RS coordinated. While these studies do not confirm this hypothesis, it is clear empirically that addition of the RS does narrow the absorption band of the dye on the TiO2 surface. The onset of absorption (λ_{onset}) is used to calculate the excited state oxidation potential $(E_{(S+/S^*)})$ via the equation $E_{(S+/S^*)} = E_{(S+/S)} - E_g^{\text{opt}}$, where $E_{(S+/S)}$ is the ground state oxidation potential found via cyclic voltammetry (CV) and $E_{\rm g}^{\rm opt}$ is the optical gap found by converting $\lambda_{\rm onset}$ from nm to eV. The λ_{onset} was mathematically found to be 581 nm via the "Onset" program. The $E_{(S+/S)}$ value of **DN1** was found from CV to be 1.22 V versus normal hydrogen electrode (NHE) in

dichloromethane solution with tetrabutylammonium hexafluorophosphate as the supporting electrolyte (Figure S1). The oxidation potential of $[Co(PY5Me_2)(L)]^{3+/2+}$ is reported to be 0.78 V versus NHE in the presence of the common DSC device additive tert-butylpyridine (TBP)²⁶ (or at 0.82 V in the absence of TBP where L is MeCN, Figure S2). Thus, the $E_{(S+/S)}$ value of **DN1** is sufficiently positive to drive a favorable electron transfer reaction between the oxidized dye and $[Co(PY5Me_2)(L)]^{2+}$. The $E_{(S+/S)}$ and absorption curve onset lead to an $E_{(S+/S^*)}$ value of -0.91 V, which is sufficiently negative for favorable electron injection into the TiO2 conduction band, taken as -0.5 V, as is commonly used in the DSC literature. From the optical and electrochemical data, it is apparent that DN1 is well-positioned energetically for facile electron injection into the TiO2 conduction band with a driving force of injection (ΔG_{inj}) of 410 mV and for a facile electron transfer reaction from $[Co(PY5Me_2)(L)]^{2+}$ at a regenerative driving force (ΔG_{reg}) of 440 mV (Figure 3).

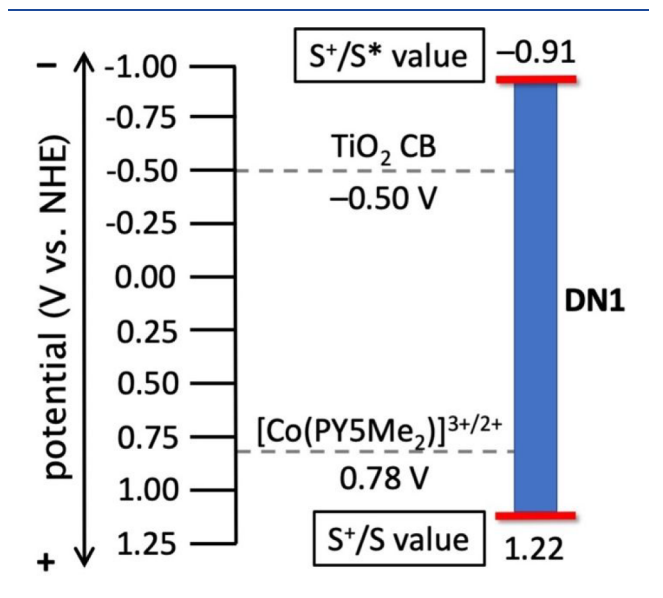


Figure 3. Potential energy diagram of **DN1** relative to the conduction band of TiO_2 and $[Co(PY5Me_2)(L)]^{3+/2+}$ in the presence of TBP.

Transient absorption spectroscopy (TAS) experiments were conducted on TiO2-bound DN1 films to observe both the duration of photoinduced charge separation after electron injection in the absence of the RS and the rate of electron transfer from [Co(PY5Me₂)(L)]²⁺ to the oxidized dye. The TAS studies herein are done on a microsecond time scale where electron injection is assumed to be completed so that the main signals observed are from the oxidized dye. For the LA-LB approach to have a significant influence on DSC device performances, an LA-LB rate enhancement must be evident in the presence of a complex electrolyte system such as is used in DSC devices, which includes the oxidized RS, the reduced RS, LiTFSI (lithium bis(trifluoromethane)sulfonimide), and TBP—an additive that serves several key functions in the device. 33,34 The full regenerative electrolyte in this study is comprised of 0.25 M Co²⁺, 0.05 M Co³⁺, 0.1 M LiTFSI, and 0.5 M TBP. We note that this electrolyte environment is complex; however, the full electrolyte is required for more realistic measurements when assessing the regeneration efficiency of a DSC device (vide infra). TAS studies using complex electrolytes are common in the DSC field for this reason.^{3,4,35} Thus, in these studies, 0.1 M LiTFSI and 0.5 M TBP are held constant, while the charge separation duration and regeneration rates are probed without and with the Co complexes being present, respectively.

TAS measurements in the absence of the RS show a strong absorbance at 720 nm, which is assigned to the dye cation along with a ground state bleach (GSB) near 450 nm (Figure 4, Table 1). The TAS signal decay kinetics at 720 nm were fit

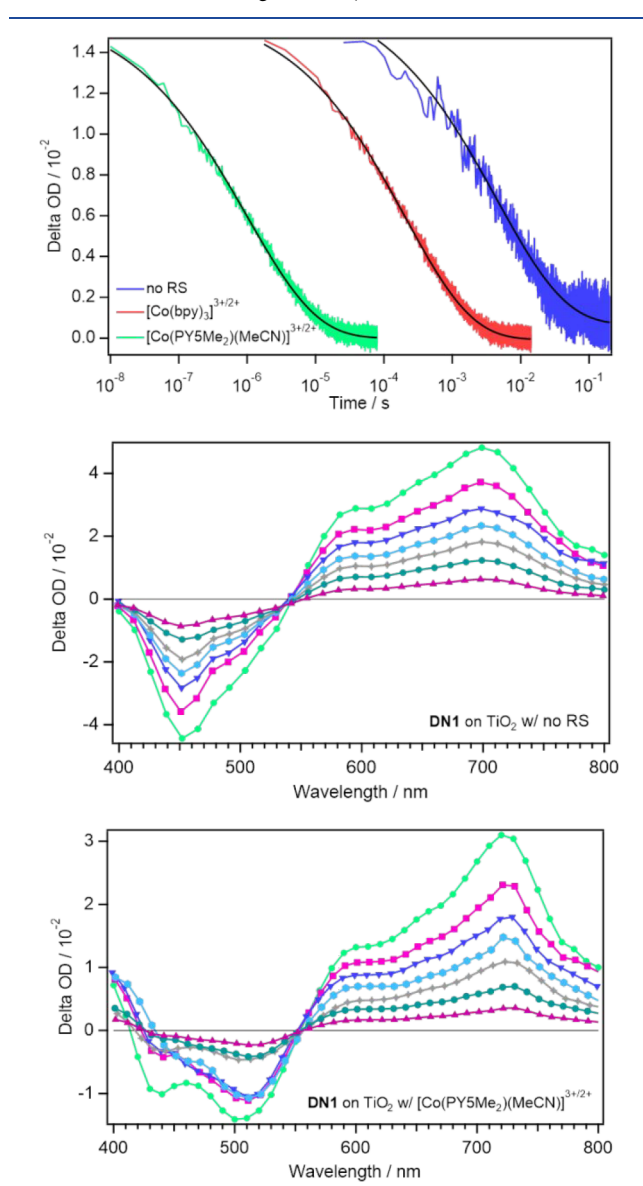


Figure 4. Top: Transient decay signals at 720 nm corresponding to TiO_2 -bound **DN1**, TiO_2 -bound **DN1** with added $[CoPYSMe_2)-(MeCN)]^{3+/2+}$, and TiO_2 -bound **DN1** with added $[Co(bpy)_3]^{3+/2+}$. Middle: TA spectrum of **DN1** on TiO_2 with no RS present. Bottom: TA spectrum of **DN1** on TiO_2 with $[Co(PYSMe_2)(MeCN)]^{3+/2+}$.

with a stretched exponential Kohlrausch–Williams–Watts (KWW) function. $^{36-39}$ The use of a KWW fitting approach is commonly used in the DSC literature, in part, because it can accommodate the complexity of signals with multiple rate components within complex DSC environments. $^{40-43}$ A photoinduced interfacial charge separated state lifetime of 1.2×10^{-3} s is observed between reduced TiO_2 and the oxidized

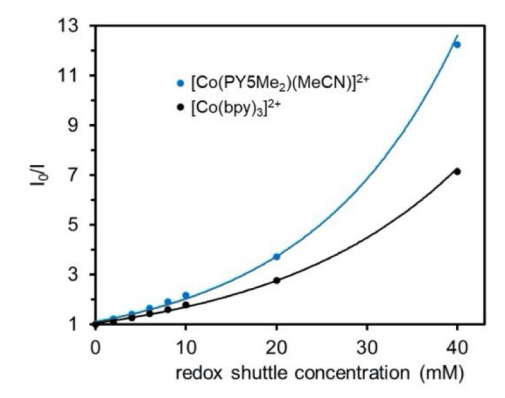
dye (TiO₂(e)⁻ldye⁺). This corresponds to a back electron transfer (BET) rate of $8.6 \times 10^2 \, \mathrm{s}^{-1}$. Upon introduction of the RS (both Co²⁺ and Co³⁺ states), a similar TAS spectrum is observed of the dye cation with a substantially shorter dye cation lifetime of 1.8×10^{-6} s, which can be attributed to rapid electron transfer from the Co2+ species to the oxidized dye. Notably, neither oxidation state of the $[Co(PY5Me_2)(L)]$ RS absorbs past ~650 nm, which allows for direct monitoring of the dye cation signal (Figure S3).44 The corresponding rate of dye cation signal decay is $5.5 \times 10^5 \text{ s}^{-1}$ (Figure 4). The regeneration rate (k_{reg}) is substantially faster than the BET rate (k_{BET}) , which leads to a regeneration efficiency (Φ_{reg}) of 99.8% using the equation $\Phi_{\text{reg}} = (k_{\text{reg}}/(k_{\text{reg}} + k_{\text{BET}})) \times 100\%$ (Table 1). 35,43 As has been previously noted, this commonly used approach to estimating Φ_{reg} likely overestimates the often complex-to-obtain absolute Φ_{reg} value acquired from the electron transfer reactions; however, this approach works well for the comparison of Φ_{reg} obtained under similar experimental conditions.

As a control, $[Co(bpy)_3]^{3+/2+}$ was used as an RS, which does not have an open or labile coordination site available to bind to **DN1**. The lifetime of the dye cation is observed at 5.8×10^{-4} s for a signal decay rate of $1.7 \times 10^3 \text{ s}^{-1}$, which is more than 2 orders of magnitude slower than the dye cation signal decay rate when $[Co(PY5Me_2)(L)]^{3+/2+}$ is employed (Figures 4 and S7). The dramatic change in rates can be attributed to the generation of a transient LA-LB bonding interaction between the surface-bound dye and $[Co(PYSMe_2)(L)]^{3+/2+}$, which is unlikely to be formed with $[Co(bpy)_3]^{3+/2+}$. The Φ_{reg} of DN1 with the $[Co(bpy)_3]^{3+/2+}$ electrolyte is calculated to be 66.4%, which is significantly lower than the 99.8% value obtained with $[Co(PY5Me_2)(L)]^{3+/2+}$. As an additional control, dye A1 with no pyridyl groups was synthesized according to literature procedures (Figure 1).20 Interestingly, the dye cation decay rate was faster with the [Co(bpy)₃]^{3+/2+} electrolyte than the $[Co(PY5Me_2)(L)]^{3+/2+}$ electrolyte with A1 (1.0×10^6) versus 1.1×10^4 s⁻¹, Table 1, Figures S10 and S11). This suggests a favorable interaction between DN1 and [Co(PY5Me2)- $(L)^{3+/2+}$ is occurring, since this system shows the inverse trend.

The binding of the dye to the $[Co(PY5Me_2)(MeCN)]^{2+}$ RS was further probed in homogeneous solution studies through the synthesis of the methyl ester derivative of DN1 (DN1ester). DN1-ester was synthesized to eliminate any potential hydrogen bonding of the CAA group on the acceptor region with the pyridine groups on the donor region of the dye, which could complicate the results (Scheme S1). To probe the dye-RS interactions, Stern-Volmer plots with emission quenching were generated with the dye in the presence of added $[Co(PY5Me_2)(MeCN)]^{2+}$ with a comparison to $[Co(bpy)_3]^{2+}$ (Figures 5, S4, and S5). ^{48,49} Nonlinear emission quenching was observed when [Co(PY5Me₂)(MeCN)]²⁺ was added at concentrations of the RS significantly lower than those present in an operational DSC device. Co RSs are typically present in DSC devices at a concentration of ~0.25 M for highperformance devices; however, these concentrations lead to complete quenching. The highest concentration of the RS shown on the graph (40 mM) resulted in a substantial quenching of emission with higher concentrations of the RS giving no appreciable emission (Figure S4). A similar nonlinear emission quenching profile is observed for [Co(bpy)₃]²⁺ at approximately half the quenching ratio observed for [Co- $(PY5Me_2)(MeCN)]^{2+}$ at the highest concentration probed (40

Table 1. Lifetimes and Rates of Photogenerated Dye Cation Signal Decays Found via TAS Experime	Table 1	. Lifetimes and R	ates of Photogenerated	d Dve Cation Sig	mal Decays Found	l via TAS Experiment
--	---------	-------------------	------------------------	------------------	------------------	----------------------

dye	RS	$ au_{ m obs} \ (m s)$	$k_{\rm obs}~({\rm s}^{-1})$	$\Phi_{ m reg}~(\%)$
DN1	none	1.2×10^{-3}	8.6×10^{2}	
DN1	$[Co(PY5Me_2)(L)]^{3+/2+}$	1.8×10^{-6}	5.5×10^5	99.8
DN1	$[Co(bpy)_3]^{3+/2+}$	5.8×10^{-4}	1.7×10^{3}	66.4
DN1-ester	$[Co(bpy)_3]^{2+}$	2.0×10^{-7}	5.0×10^{6}	
DN1-ester	$[Co(bpy)_3]^{3+}$	$>1.0 \times 10^{-2}$	$<1.0 \times 10^{2}$	
DN1-ester	$[Co(PY5Me_2)]^{2+}$	9.4×10^{-7}	1.1×10^{6}	
DN1-ester	$[Co(PY5Me_2)]^{3+}$	2.5×10^{-4}	4.0×10^{3}	
A1	none	4.0×10^{-4}	2.5×10^{3}	
A1	$[Co(PY5Me_2)(L)]^{3+/2+}$	9.2×10^{-5}	1.1×10^{4}	81.5
A1	$[Co(bpy)_3]^{3+/2+}$	1.0×10^{-6}	1.0×10^{6}	99.8



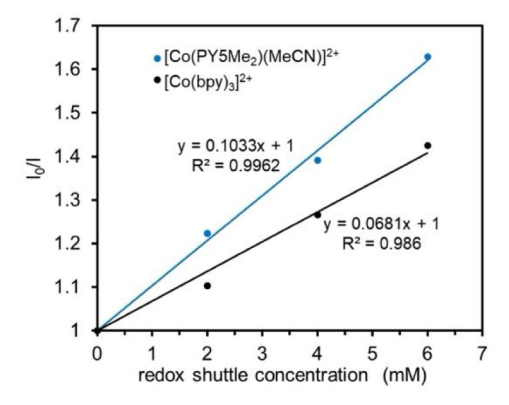


Figure 5. Stern-Volmer quenching plot for DN1-ester at a 5 μ M concentration in acetonitrile with high (top) and low (bottom) concentrations of the RSs.

mM, Figures 5 and S5). The nonlinearity of both the Co²⁺ RSs in quenching the emission of DN1-ester suggests nondiffusional behavior for the dye and both RS quencher pairs. The nonlinear quenching with added [Co(PY5Me₂)(MeCN)]²⁺ is predicted due to LA-LB binding; however, the origin of nonlinear quenching with added $[Co(bpy)_3]^{2+}$ is not obvious. Emission quenching is significantly more effective with added [Co(PY5Me₂)(MeCN)]²⁺ presumably due to LA-LB binding, which is consistent with the TAS experimental results. At low concentrations (2-6 mM) of the RSs, a near linear relationship is observed in the Stern-Volmer plot with Stern-Volmer quenching constants (K_{SV}) of 0.103 and 0.068 for the [Co(PY5Me₂)(MeCN)]²⁺ and [Co(bpy)₃]²⁺ RSs, respectively (Figure 5). The higher quenching constant upon addition of the [Co(PY5Me₂)(MeCN)]²⁺ complex is correlated to a faster electron transfer reaction from [Co(PY5Me₂)(L)]²⁺ to the dye cation as observed via surface TAS studies. It is important to

note that there are multiple emission quenching pathways available such as paramagnetic quenching, and the quenching constants may contain other emission loss pathways beyond electron transfer reactions.⁵⁰

¹H NMR studies were undertaken in an attempt to examine binding of [Co(PY5Me₂)(MeCN)]²⁺ to DN1-ester (Figures S24-S26). A broadening of the DN1-ester signals is observed as [Co(PY5Me₂)(MeCN)]²⁺ is added. This does not confirm binding of DN1-ester to [Co(PY5Me₂)(MeCN)]²⁺, but it is interesting to note that the tetramethylsilane in the ¹H NMR experiments retains a sharp peak shape regardless of [Co-(PY5Me₂)(MeCN)]²⁺ concentration. The selective broadening of the DN1 peaks in the presence of [Co(PY5Me₂)-(MeCN)]²⁺ suggests an interaction between these two species. Additionally, a ratio of DN1-ester fluorescence intensity without and with [Co(PY5Me2)(MeCN)]2+ plotted against the mole fraction of the total analyte (dye plus redox shuttle) shows no significant quenching of the emission intensity from the dye at 1×10^{-5} M regardless of mole fraction (Figures S27 and S28). This suggests that if a binding interaction of the redox shuttle to the dye is taking place, the binding is a weak interaction with an equilibrium possibly favoring nonbinding of the cobalt complex to the dye at these concentrations. Higher concentrations of the cobalt complex were needed to observe fluorescence quenching, such as those used in the Stern-Volmer studies above.

The DN1-ester binding to [Co(PY5Me₂)]²⁺ was also probed computationally at the ω -B97XD⁵¹/6-31+G(d)^{52,53} level of theory for all atoms except the Co atom, which utilizes the LANL2TZ(f) basis set (see the Experimental Section for additional details).⁵⁴ The cobalt complex was placed within bonding distance to each of the nitrogen and sulfur heteroatoms of DN1-ester, and the structure was then allowed to optimize geometrically. No low-energy geometry was found for the binding of the cobalt complex to either sulfur atom of DN1-ester. The cobalt complex, instead, moves to either the pyridyl nitrogens or the cyano nitrogen as a minimum energy geometry. The choice depends upon which sulfur atom the cobalt complex was initially attempted to bond with at the beginning of the optimization computation. Additionally, no low-energy geometry was found with respect to the triarylamine nitrogen, presumably due to the steric environment around the amine, and the cobalt complex moved to the pyridyl nitrogens as a low-energy complex. The two low-energy geometries are effectively degenerate with one another, since the relative energies are within ~9 kcal/mol of each other. These structures are shown in Figure 6 with binding of the cobalt complex to either a pyridyl nitrogen or the cyano nitrogen. In a functional DSC device where the carboxylic acid

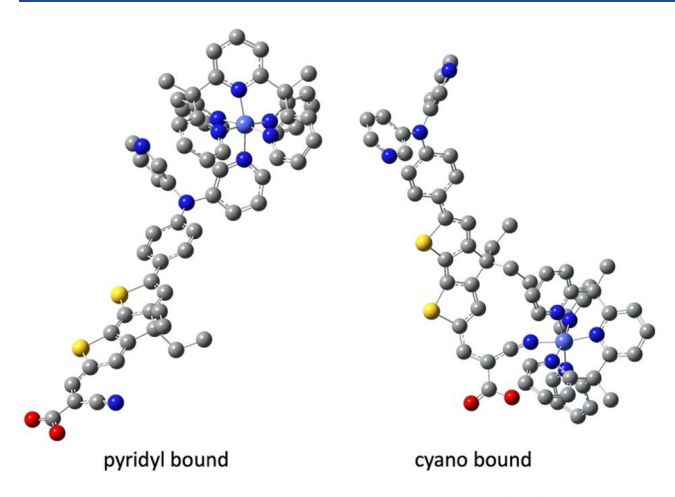


Figure 6. Optimized geometries of pyridyl-bound (left) and cyanobound (right) **DN1-ester** with $[Co(PY5Me_2)]^{2+}$. Hydrogen atoms are omitted for clarity.

group is bound to a TiO2 surface, the binding of the cobalt complex to a cyano group is not likely due to steric constraints. Thus, only the pyridyl nitrogens lead to a reasonable binding of the cobalt complex to DN1. A computed bond distance of 1.85 Å is observed from the **DN1**-pyridyl nitrogen to the Co center. The Co-N_{ligand} bond length trans to the dye-N-Co bond is 1.88 Å, and all the remaining Co-N_{ligand} bond lengths are \sim 1.82 Å. Thus, the bond length from the Co center to the dye is similar to the PY5Me2 ligand Co-N bond lengths. A potential cause of the weak binding observed in the fluorescence quenching studies described above could be due to the steric environment at the pyridyl groups. The nonbinding pyridyl group has a carbon atom within 3.2 Å of another carbon atom of the pentadentate ligand on the cobalt atom. This type of steric congestion likely weakens the dyecobalt complex binding, which could be beneficial in a DSC device where the redox shuttle should be transiently bound.

Additional solution-phase TAS studies were undertaken with **DN1-ester** and the Co²⁺ complexes with significantly simplified conditions relative to the film studies (Figures S8 and S9, Tables 1). Upon photoexcitation with only dye and RS present in solution, an electron transfer reaction may occur according to eq 1

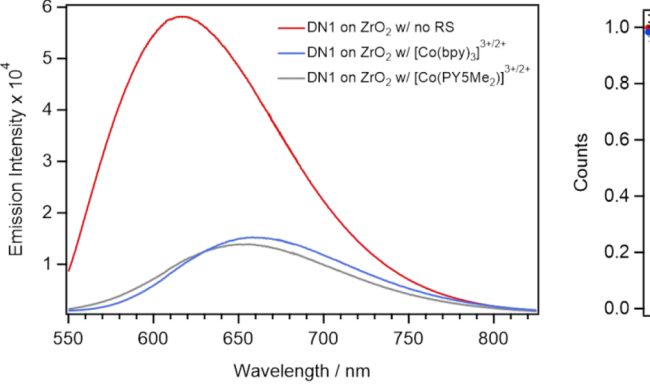
DN1-ester +
$$Co^{3+}$$
 + $h\nu \rightarrow [$ **DN1-ester** $]^{+}$ + Co^{2+} (1)

$$[\mathbf{DN1\text{-ester}}]^+ + \mathbf{Co}^{2+} \to \mathbf{DN1\text{-ester}} + \mathbf{Co}^{3+}$$
 (2)

DN1-ester +
$$Co^{2+}$$
 + $h\nu \rightarrow [\mathbf{DN1\text{-ester}}]^{+}$ + Co^{+} (3)

The transient absorption spectra are very similar to that observed for DN1 on TiO2 and via spectroelectrochemistry (SEC) measurements on **DN1-ester** (Figure S6). The electron transfer reaction in eq 2 is similar to the electron transfer reaction occurring at the TiO2 surface referred to as regeneration. With DN1-ester, the electron transfer reaction between the photogenerated DN1-ester cation and $[Co-(PY5Me_2)(L)]^{2+}$ is observed to be faster than with $[Co-(PY5Me_2)(L)]^{2+}$ $(bpy)_3]^{2+}$ (dye cation decay rates of $4.0 \times 10^3 \text{ s}^{-1}$ versus < 1.0 \times 10² s⁻¹), which can be explained by LA-LB interactions of the DN1-ester cation and [Co(PY5Me₂)(L)]²⁺. An LA-LB interaction would keep the dye and cobalt complex in close proximity for increased electron transfer reaction rates. Since the oxidative quenching of photoexcited DN1-ester is thermodynamically favorable with [Co(PY5Me₂)(L)]²⁺ by 80 mV,55 TAS experiments with DN1-ester and added [Co-(PY5Me₂)(MeCN)]²⁺ were undertaken as well, which show the formation of the DN1-ester cation with a relatively rapid decay rate of $1.1 \times 10^6 \text{ s}^{-1}$ (eq 3 and Table 1). Notably, this electron transfer reaction is not desirable within a DSC device, since the photoexcited dye would ideally be oxidatively quenched by TiO2. This suggests a potential DSC device performance limitation, which could be circumvented through the future design of dyes and RSs that do not thermodynamically favor oxidative quenching of the photoexcited dye. Similarly, DN1 was examined on insulating ZrO2 films via emission quenching studies both under steady-state and timeresolved conditions (Figure 7). Under these conditions with the redox shuttles present in the same amounts as in functional DSC devices (0.25 M Co²⁺ and 0.05 M Co³⁺), **DN1** emission is quenched at near equal amounts with both $[\text{Co(bpy)}_3]^{3+/2+}$ and $[\text{Co(PY5Me}_2)(L)]^{3+/2+}.$ A slightly stronger quenching in the presence of $[Co(PY5Me_2)(L)]^{3+/2+}$ is observed. Timecorrelated single photon counting experiments suggest a similar trend with emissive lifetimes of 0.9 ns without RS, 0.5 ns with $[Co(bpy)_3]^{3+/2+}$, and 0.4 ns with $[Co(PY5Me_2)-$ (L)]^{3+/2+}.

DSC devices were fabricated with **DN1**, and photovoltaic performances were measured under AM 1.5G solar simulated conditions and under fluorescent lighting conditions (Figure 8, Table 2). Power conversion efficiencies (PCEs) of each device were obtained from the equation PCE = $(J_{SC}*V_{OC}*FF)/I_0$,



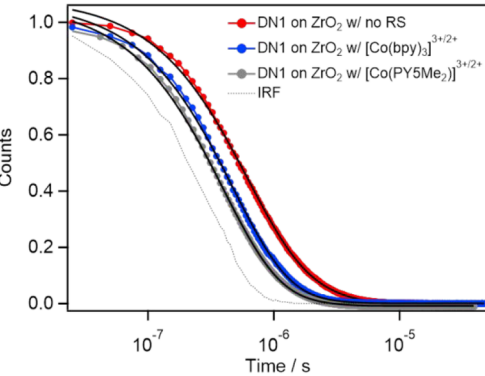


Figure 7. Steady-state emission spectrum (left) and time-correlated single photon counting curves (right) of DN1 with and without redox shuttles present in the same concentration as in functional DSC devices. IRF stands for instrument response function.

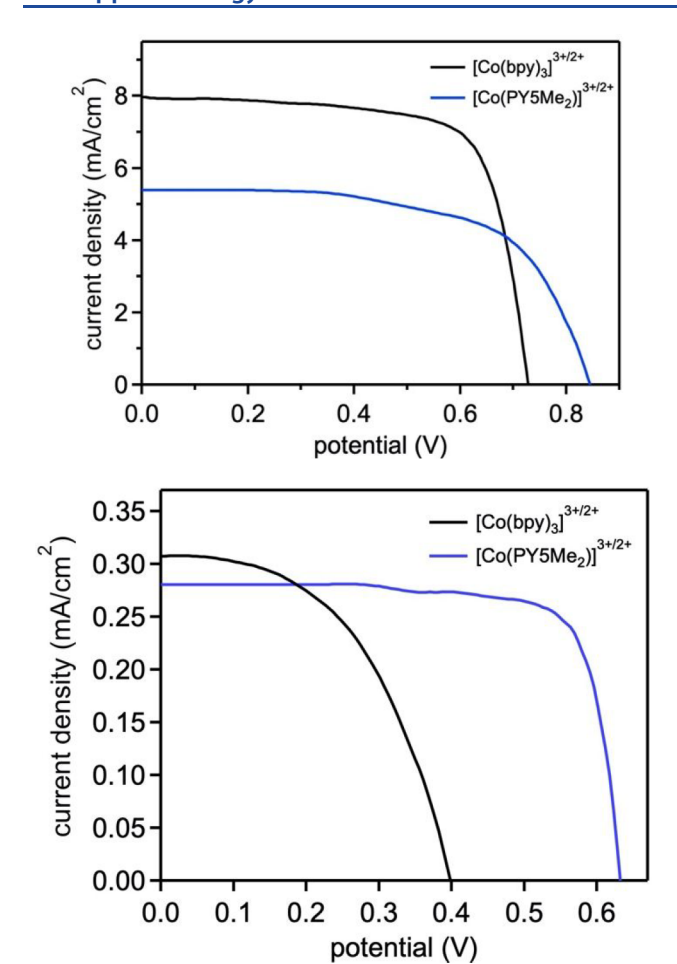


Figure 8. J-V curves of DSCs based on **DN1** at 1000 W/m² with a solar simulator (top) and 10.8 W/m² (6000 lx) with fluorescent lighting (bottom).

where J_{SC} is the short-circuit current density, V_{OC} is the open-circuit voltage, FF is the fill factor, and I_0 is the irradiation intensity. Devices with the $[\text{Co}(\text{PY5Me}_2)(\text{L})]^{3+/2+}$ RS have a V_{OC} of 835 mV, a J_{SC} of 5.5 mA/cm², and an FF of 63% for a PCE of 2.9% under full sun illumination (1000 W/m²). Notably, a higher photocurrent is observed for devices with $[\text{Co}(\text{bpy})_3]^{3+/2+}$ despite a higher regeneration efficiency being observed for the electron transfer reaction from $[\text{Co}(\text{PY5Me}_2)(\text{L})]^{2+}$ to oxidized **DN1**. Presumably, the oxidative quenching of photoexcited **DN1** by a bound $[\text{Co}(\text{PY5Me}_2)(\text{L})]^{3+}$ complex as shown by TAS studies (*vide supra*) leads to

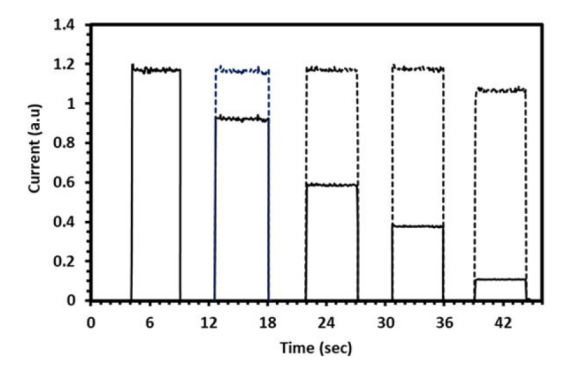
nonproductive photoinduced electron transfer reactions, which lower the peak incident photon-to-current conversion efficiency (IPCE) value and reduces photocurrent (Figure S14). A maximum $V_{\rm OC}$ ($V_{\rm OC}^{\rm max}$) of 1.28 V is possible based on the $[Co(PY5Me_2)(L)]^{3+/2+}$ RS potential when the conduction band of TiO₂ is taken to be -0.5 V. The $V_{\rm OC}$ loss ($V_{\rm OC}^{\rm loss}$) of this system is calculated according to the equation $V_{\rm OC}^{\rm loss}$ = $V_{\rm OC}^{\rm max} - V_{\rm OC}$ to be 440 mV. A lower $V_{\rm OC}$ is observed when $[{\rm Co(bpy)_3}]^{3+/2+}$ is used as the RS with a $V_{\rm OC}^{\rm loss}$ of 330 mV. The lower $V_{\rm OC}^{\rm loss}$ value with a lower observed $V_{\rm OC}$ is due to the less positive potential of $[Co(bpy)_3]^{3+/2+}$ when compared with [Co(PY5Me₂)(MeCN)]^{3+/2+}. Notably, electrochemical impedance spectroscopy suggests the two DSC devices with each RS system have similar electron lifetimes in TiO2, which indicates that any LA-LB interactions occurring at the TiO₂dye surface are not leading to appreciably faster recombination reactions (electron transfer reactions from the TiO2-dye interface to the oxidized RS) despite a presumably higher RS concentration at the TiO2-dye interface for [Co(PY5Me2)- $(L)^{3+/2+}$ (see SI Figures S12 and S13 and Table S1). The higher photocurrent and fill factor when [Co(bpy)₃]^{3+/2+} is used relative to $[Co(PY5Me_2)(MeCN)]^{3+/2+}$ results in an overall higher PCE of 4.3% at full sun (1000 W/m²) irradiation. However, when the irradiation intensity is reduced to 10% sun (100 W/m²), the PCE values of DSC devices with $[Co(PY5Me_2)(MeCN)]^{3+/2+}$ and $[Co(bpy)_3]^{3+/2+}$ are the same at 3.0%. The decrease in relative PCE value for [Co(bpy)₃]^{3+/2+} is due to a faster decrease in photocurrent and fill factor than is observed with [Co(PY5Me2)-(MeCN)]3+/2+ as the irradiation intensity is changed from full sun intensity to 10% sun intensity.

Current dynamic measurements at variable light intensities were undertaken to better understand the change in performance as a function of light intensity for the two systems (Figure 9). For these current dynamic measurements, the light source is shuttered on and off with varied light filters. The current response toward on/off light cycling can show mass transport limitations within the system if an initial spike is observed upon opening the shutter. 57,58 This initial spike occurs due to the rapid consumption of the reduced RS species at the TiO₂ surface with slow diffusion, which depletes the needed reducing RS concentration near dye cations. [Co(bpy)₃]^{3+/2+} shows no evidence of mass transport issues at any irradiation intensity; however [Co(PY5Me₂)(MeCN)]^{3+/2+} has clear evidence of current limited mass transport with a 30% decrease in current from the initial high current spike to the steady-state plateau of photocurrent at 100% sun irradiation intensity.

Table 2. DSC Device Data with DN1a

RS	irradiation intensity	irradiation source	$V_{\rm oc}~({ m mV})$	$J_{\rm sc} \left({\rm mA/cm^2}\right)$	FF (%)	PCE (%)
$[Co(PY5Me_2)(L)]^{3+/2+}$	1000 W/m ² (100% sun)	solar simulator	835	5.5	63	2.9
$[Co(bpy)_3]^{3+/2+}$	$1000 \text{ W/m}^2 (100\% \text{ sun})$	solar simulator	731	8.1	73	4.3
$[Co(PY5Me_2)(L)]^{3+/2+}$	$100 \text{ W/m}^2 (10\% \text{ sun})$	solar simulator	752	0.58	60	3.0
$[Co(bpy)_3]^{3+/2+}$	$100 \text{ W/m}^2 (10\% \text{ sun})$	solar simulator	625	0.76	53	3.0
$[Co(PY5Me_2)(L)]^{3+/2+}$	25.4 W/m ² (13000 lx)	fluorescent	645	0.65	74	12.4
$[Co(bpy)_3]^{3+/2+}$	25.4 W/m ² (13000 lx)	fluorescent	481	0.71	55	7.3
$[Co(PY5Me_2)(L)]^{3+/2+}$	$10.8 \text{ W/m}^2 (6000 \text{ lx})$	fluorescent	625	0.28	73	13.0
$[Co(bpy)_3]^{3+/2+}$	$10.8 \text{ W/m}^2 (6000 \text{ lx})$	fluorescent	400	0.31	49.4	5.6
$[Co(PY5Me_2)(L)]^{3+/2+}$	$5.3 \text{ W/m}^2 (2300 \text{ lx})$	fluorescent	565	0.07	82.5	9.4

^aThe electrolyte comprises of 0.25 M Co²⁺, 0.05 M Co³⁺, 0.1 M LiTFSI, and 0.5 M TBP in acetonitrile. A PEDOT counter electrode was used in all devices. Values are the average of at least two devices with a ± 0.3 variance of PCE.



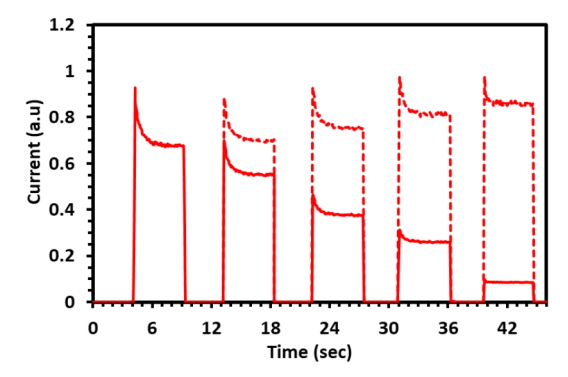


Figure 9. Current dynamics of **DN1** with $[Co(bpy)_3]^{3+/2+}$ (top) and $[Co(PY5Me_2)(L)]^{3+/2+}$ (bottom). Sun intensities are 100%, 78%, 50%, 32%, and 10% from left to right on each graph with the lamp shuttered on/off. The dashed lines are found by normalizing the data to sun intensity so that relative efficiency of current generated can be easily compared across the varied intensities. ^{57,58}

Upon changing sunlight intensities to lower values, the magnitude of the decrease in photocurrent output from the spike to the steady-state plateau decreases significantly from a 30% drop at 100% sun intensity to a 10% drop at 10% sun intensity. This indicates that as irradiation intensity is decreased, $[Co(PY5Me_2)(L)]^{3+/2+}$ becomes more kinetically competent at reaching steady-state redox cycling in the DSC device allowing for higher quantum yields for the completed device circuit. Current dynamics measurements at varied light intensity also provide information about the proportional current response at varied light intensity. In Figure 9, the dashed lines are the current responses normalized based on light intensity. For the case of $[Co(PY5Me_2)(L)]^{3+/2+}$, the photocurrent response is highest when normalized to light intensity at 10% sun intensity. The opposite is observed in the case of $[Co(bpy)_3]^{3+/2+}$ with 10% sun intensity providing the least amount of photocurrent. These trends suggest that the LA-LB approach using $[Co(PY5Me_2)(MeCN)]^{3+/2+}$ could be valuable for indoor photovoltaics in fluorescent-light-to-electric applications.

Fluorescent-light-generated J-V curve measurements on the DSC devices were undertaken with a OSRAM 930 warm-white fluorescent light source (bulb 011318), which has a commonly used emission range with a 750 nm onset and has been used in prior reports on fluorescent light studies.³ DSC devices with $[\text{Co}(\text{PYSMe}_2)(\text{L})]^{3+/2+}$ have a peak performance of 13.0% PCE at 6000 lx with similar performance at 13 000 lx. The PCE of these devices begins to decrease at 2300 lx to 9.4%. DSC devices with $[\text{Co}(\text{bpy})_3]^{3+/2+}$ show dramatically lower

PCE values at all indoor lighting intensities. A 13 000 lx intensity leads to a 7.3% PCE, which decreases to 5.6% at 6000 lx and does not give a J-V curve on our instrumentation at 2300 lx. Under these low-light conditions, diffusion (or mass transport) is no longer current limiting under steady-state irradiation for the $[\text{Co}(\text{PY5Me}_2)(\text{L})]^{3+/2+}$ RS. In this environment, the LA–LB approach has a clear advantage leading to higher performing devices (13.0% versus 5.6% at 6000 lx) than $[\text{Co}(\text{bpy})_3]^{3+/2+}$, which was non-operable at extremely low-light intensity. Thus, dye–RS self-assembly design approaches are valuable toward improving indoor photovoltaics performances.

CONCLUSION

A dye with Lewis base functionality was designed and synthesized with pyridine groups on the donor portion of the donor- π bridge-acceptor dye. The dye optical and electronic properties were examined via absorption spectroscopy and cyclic voltammetry. Evidence suggesting a redox shuttle with a Lewis acid site may be binding to the dye was observed using absorption spectroscopy and fluorescence spectroscopy via Stern-Volmer plots. Transient absorption spectroscopy reveals the redox shuttle with a labile coordination site that functions as a Lewis acid site, [Co(PY5Me₂)(L)]²⁺, underwent a faster electron transfer reaction with the dye when photoexcited at a TiO2 surface by >2 orders of magnitude when compared to a redox shuttle without an obvious Lewis acid site, [Co(bpy)₃]²⁺. Similar electron transfer reaction kinetic observations were made via TAS measurements on an esterified dye in solution. DSC devices were fabricated with the dye and the two redox shuttles. At full sun conditions, $[Co(PY5Me_2)(L)]^{3+/2+}$ -based devices gave inferior PCE values (about 2× lower) when compared to $[Co(bpy)_3]^{3+/2+}$ -based devices. Current dynamic studies reveal a mass transport limitation with [Co(PY5Me2)-(L) $]^{3+/2+}$ at full sun, which is likely due to slow diffusion of the redox shuttle because of Lewis acid-Lewis base interactions at the surface. However, fluorescent lighting studies reveal significantly higher PCE values with $[Co(PY5Me_2)(L)]^{3+/2+}$ based devices relative to those with $[Co(bpy)_3]^{3+/2+}$ (13.0%) versus 5.6%, respectively). Under these low-light conditions, mass transport was not current limiting, which allowed for the improved electron transfer reaction rates of the Lewis acid-Lewis base self-assembly approach to demonstrate higher performances. This approach is valuable for low-light conditions such as those used for indoor photovoltaics and in tandem or multijunction DSC systems. Intriguingly, this approach has led to reasonable performances with a cobalt redox shuttle under low-light conditions where the commonly utilized [Co(bpy)₃]^{3+/2+} underperforms. Notably, recombination rates as measured by electrochemical impedance spectroscopy do not seem to increase with the use of the Lewis acid-Lewis base coordination approach pursued with [Co- $(PY5Me_2)(L)^{3+/2+}$ despite the presumably higher local concentration of the redox shuttle near the TiO2 surface. Future studies focused on designing a dye with electronically and sterically altered Lewis basic functionality to vary binding strength and for better fluorescent lighting spectral overlap is underway, since the current dye ceases to absorb photons approximately 150 nm (about 42% of the spectrum) before common fluorescent lighting systems stop emitting.

EXPERIMENTAL SECTION

General Information. All commercially obtained reagents were used as received. N-Phenyl-N-(pyridin-3-yl)pyridin-3-amine²⁷ and tributyl(4,4-dihexyl-4*H*-cyclopenta[2,1-*b*:3,4-*b*']dithiophen-2-yl) stannane²⁸ were synthesized as previously reported in the literature. [Co(bpy)₃](PF₆)₃ and [Co(bpy)₃](PF₆)₂ were synthesized according to a literature procedure. [Co(PY5Me₂)](OTf)₂ and [Co-(PY5Me₂)](OTf)₂(TFSI) (where OTf is trifluoromethanesulfonate) were prepared as previously reported.²⁶ All reactions were carried out under nitrogen unless otherwise noted. Thin-layer chromatography (TLC) was conducted with sorbent silica XHL TLC plates and visualized with a 254 nm UV lamp. Column chromatography was performed using Sorbent Technologies, Inc. silica gel, porosity 60 Å, $40-63 \mu m$ (230 × 400 mesh). ¹H NMR spectra were recorded on a Bruker Avance 400 (400 MHz) spectrometer and reported in ppm using the protiated solvent as an internal standard (CDCl3 at 7.26 ppm, (CD₃)₂SO at 2.50 ppm, CD₃CN at 1.94 ppm). Peaks are reported as (s = singlet, d = doublet, t = triplet, q = quartet, m = multiplet; coupling constant (Hz); integration). Absorbance spectra were measured with a Cary 5000 UV-vis-NIR spectrometer with dichloromethane solutions. Cyclic voltammetry curves were measured with a C-H Instruments Electrochemical Analyzer (Model CHI602E). Measurements were taken using a platinum counter electrode, a Ag/ AgCl reference electrode, and a glassy carbon working electrode. The electrolyte solution used was 0.1 M Bu₄NPF₆ in dichloromethane. Ferrocene was used as the reference standard and taken as 0.70 V versus normal hydrogen electrode (NHE) in DCM, and oxidation potentials are recorded versus NHE in dichloromethane. FT-IR experiments were recorded on a Bruker Alpha FT-IR spectrometer. For electrospray ionization (ESI) high-resolution mass spectrometry (HRMS), quadruple-TOF was used to obtain the data both in positive and negative mode with a Waters Synapts XS. With respect to solution steady-state emission studies, spectra were collected with a Horiba Scientific Fluoromax+ Spectrophotometer (model: Fluoromax-Plus-C). With respect to film emission studies, steady-state emission spectra were obtained with the 485 nm line of a pulsed diode laser (PicoQuant PDL 800-B), a spectrograph (Princeton Instruments Acton SP2500), and CCD camera (Princeton Instruments ProEM). Fluorescence lifetimes were acquired with an avalanche photodiode. A 550 nm long-pass filter (Thorlabs FGL550) was used for all measurements.

Computational Methods. The geometries of the molecular structures in question are optimized via density functional theory with the ω -B97XD functional⁵¹ utilizing the 6–31+G(d) basis set^{52,53} for all atoms save for the Co atom, which utilizes the LANL2TZ(f) basis set.⁵⁴ Each structure is computed with a +2 charge and a multiplicity of 4, and all computations utilize the Gaussian16 quantum chemistry program.⁵⁹ This methodology has been shown to be reliable in related, previous work.⁶⁰

The attachment of the [Co(PY5Me₂)]²⁺ group to **DN1** is attempted at five sites: on each of the nitrogen atoms (three sites: pyridyl nitrogen, triarylamine nitrogen, and cyano nitrogen) and each of the sulfur atoms (two sites: either sulfur of CPDT). The only two viable locations reaching an optimized geometry are the pyridyl nitrogens and the cyano group. The two sulfur atoms as well as the triarylamine nitrogen do not bind at their initially perscribed sites. The relative energy is determined as the difference in the optimized energy between total structures.

Synthesis. *N-(4-Bromophenyl)-N-(pyridin-3-yl)pyridin-3-amine* (2). To a flame-dried round bottom flask was added *N*-phenyl-*N*-(pyridin-3-yl)pyridin-3-amine²⁷ (2.1 g, 8.6 mmol) and anhydrous THF (48 mL). The solution was cooled to 0 °C under N₂. Then, recrystallized *N*-bromosuccinimide (1.7 g, 9.5 mmol) was added, and the reaction was stirred for 4 h. The reaction mixture was diluted with dichloromethane and then extracted with saturated aqueous Na₂CO₃ (2×) and then extracted once with water. Next, the organic layer was dried with Na₂SO₄. The product was then purified by flash chromatography with silica gel as a thin plug with acetone as the eluent to give the desired product in 64% yield (1.8 g, 5.5 mmol). ¹H

NMR (400 MHz, CDCl₃) δ 8.38 (d, J = 2.9 Hz, 2H), 8.32 (d, J = 6.1 Hz, 2H), 7.44–7.37 (m, 4H), 7.24–7.20 (m, 2H), 6.98 (d, J = 8.8 Hz, 2H). 13 C{ 1 H} NMR (400 MHz, CDCl₃) δ 145.6, 145.2, 144.6, 143.2, 133.1, 130.6, 125.8, 124.1, 117.3. IR (neat, cm $^{-1}$): 3034, 2936, 2872, 1710, 1573, 1476, 1427, 1285, 1183. HRMS ESI (positive mode) m/z calc'd for C₁₆H₁₃BrN₃ [M + H] $^{+}$: 326.0293, found 326.0260.

N-(4-(4,4-Dihexyl-4H-cyclopenta[2,1-b:3,4-b']dithiophen-2-yl)phenyl)-N-(pyridin-3-yl)pyridin-3-amine (4). Stannylated cyclopentadithiophene²⁸ (CPDT) 3 (0.58 g, 0.72 mmol), amine 2 (0.20 g, 0.60 mmol), and DMF (2.9 mL) were added into a pressure flask, and the mixture was degassed with N₂ for 30 min. Next, PdCl₂(PPh₃)₂ (21 mg, 0.03 mmol) was added, the flask was sealed, and the mixture was stirred at 90 °C overnight. Then, the reaction mixture was extracted with hexanes:diethyl ether (1:1) and water, and the organics were dried with Na2SO4. Next, the product was purified by flash chromatography with silica gel as a thin plug with hexanes and ethyl acetate as the eluents to give the product in 81% yield. (0.44 g, 0.73 mmol). ¹H NMR (400 MHz, CDCl₃) δ 8.43 (d, J = 3.0 Hz, 2H), 8.31 (d, J = 4.8 Hz, 2H), 7.57 (d, J = 8.6 Hz, 2H), 7.43 (d, J = 8.2 Hz, 2H), 7.23-7.20 (m, 2H), 7.17 (d, J = 4.8 Hz, 1H), 7.13 (s, 1H), 7.10(d, J = 8.6 Hz, 2H), 6.94 (d, J = 4.8 Hz, 1H), 1.86-1.82 (m, 4H),1.22-1.10 (m, 12H), 1.03-0.90 (m, 4H), 0.82-0.78 (m, 6H). $^{13}\text{C}\{^{1}\text{H}\}$ NMR (400 MHz, CDCl₃) δ 158.7, 157.7, 145.2, 144.4, 144.0, 143.0, 142.8, 136.3, 135.8, 131.4, 130.0, 126.3, 124.7, 124.6, 123.7, 121.4 117.3, 53.5, 37.6, 31.4, 29.5, 24.3, 22.4, 13.8. IR (neat, cm⁻¹): 2926, 2854, 1573, 1520, 1477, 1412, 1287, 1185, 1107, 1018. HRMS ESI (positive mode) m/z calc'd for $C_{37}H_{42}N_3S_2$ [M+H]⁺: 592.2820, found 592.2811.

6-(4-(Di(pyridin-3-yl)amino)phenyl)-4,4-dihexyl-4H-cyclopenta-[2,1-b:3,4-b']dithiophene-2-carbaldehyde (5). To a flame dried, N_2 filled flask was added anhydrous DMF (5.4 μ L, 0.07 mmol), CPDT 4 (40 mg, 0.07 mmol), and dichloroethane (0.2 mL). Then, the solution was cooled to 0 °C, and POCl₃ (6.7 μ L, 0.07 mmol) was added. The reaction was stirred at 0 °C for 2.5 h. Then, KOH (aq.) (0.2 mL, 1.0 M solution) was added, and the mixture was shaken vigorously for ~15 min leading to a color change from purple to orange. Next, the reaction mixture was extracted with dichloromethane and KOH (aq.). The organic layer was separated and dried with Na₂SO₄. Finally, the product was purified with flash column chromatography with silica gel using hexanes and acetone as the eluent to give the pure desired product in 44% yield (22 mg, 0.03 mmol). ¹H NMR (400 MHz, CDCl₃) δ 9.83 (s, 1H), 8.43 (s, 2H), 8.33 (d, J = 4.9 Hz, 2H), 7.58-7.56 (m, 3H), 7.45-7.43 (m, 2H), 7.24-7.23 (m,2H), 7.16 (s, 1H), 7.12-7.09 (d, J = 4.9 Hz, 2H),1.91-1.86 (m, 4H), 1.21-1.15 (m, 12H), 1.00-0.93 (m, 4H), 0.82-0.79 (m, 6H). ${}^{13}C\{{}^{1}H\}$ NMR (400 MHz, CDCl₃) δ 182.6, 163.5, 157.7, 148.5, 147.9, 145.8, 145.7, 144.6, 143.3, 143.2, 134.7, 130.8, 130.6, 130.0, 127.1, 124.4, 124.2, 117.5, 54.3, 37.8, 31.7, 29.7, 24.7, 22.7, 14.1. IR (neat, cm⁻¹): 3032, 2923, 2852, 1645, 1573, 1476, 1393, 1285, 1221, 1128. HRMS ESI (positive mode) m/z calc'd for $C_{38}H_{42}N_3OS_3$ [M+H]⁺: 620.2769, found 620.2730.

(E)-2-Cyano-3-(6-(4-(di(pyridin-3-yl)amino)phenyl)-4,4-dihexyl-4H-cyclopenta[2,1-b:3,4-b']dithiophen-2-yl)acrylic Acid (**DN1**). To a round-bottom flask was added aldehyde 5 (22 mg, 0.03 mmol) and CHCl₃ (0.5 mL). The mixture was degassed with N₂ for 30 min. Then, cyanoacetic acid (7.7 mg, 0.09 mmol) and piperidine (21 μ L, 0.21 mmol) were added into the flask. The flask was sealed with a plastic cap and electrical tape, and then, the reaction was stirred at 90 °C for 2 h. Acetic acid was added giving a color change from yellow to orange, and the mixture was extracted with dichloromethane and water. The organic layer was dried over anhydrous Na₂SO₄ and purified by flash chromatography with a thin silica gel plug using a gradient eluent mixture as follows: 5% methanol:95% DCM; 25% methanol:75% DCM; 40% methanol:60% DCM. The pure product was obtained as an orange-red compound in 84% yield (19 mg, 0.03 mmol). 1 H NMR (400 MHz, DMSO) δ 8.34–8.31 (m, 5H), 7.85 (s, 1H), 7.70-7.68 (d, J = 8.7 Hz, 2H), 7.61 (s, 1H), 7.52-7.50 (d, J =8.5 Hz, 2H), 7.40-7.36 (m, 2H), 7.10-7.08 (d, J = 8.6 Hz, 2H), 1.90-1.86 (m, 4H), 1.14-1.10 (m, 12H), 0.94-0.84 (m, 4H), 0.78-0.75 (m, 6H). No 13C NMR was taken due to apparent aggregation at

concentrations high enough to collect a spectrum in a reasonable time frame. IR (neat, cm $^{-1}$): 3480, 2925, 2206, 1568, 1411, 1367, 1288. HRMS ESI (positive mode) m/z calc'd for $C_{41}H_{43}N_4O_2S_2$ [M+H] $^+$: 687.2827, found 687.2800.

Methyl (E)-2-Cyano-3-(6-(4-(di(pyridin-3-yl)amino)phenyl)-4,4dihexyl-4H cyclopenta[2,1-b:3,4-b']dithiophen-2-yl)acrylate (DN1ester). To a round-bottom flask equipped with a stir bar, was added DN1 (0.054 g, 0.08 mmol), dry dichloromethane (23 mL), thionyl chloride (0.78 g, 6.56 mmol), and benzotriazole (0.781 g, 6.56 mmol). The reaction was then stirred for 2 h. The dichloromethane was then evaporated under reduced pressure, and methanol (23 mL) was added along with triethylamine (0.027 g, 0.272 mmol). The solution was allowed to stir at room temperature for 30 min. The methanol was evaporated, and the crude product was purified via silica gel column chromatography with 40% acetone:60% hexanes to give the product in 46% yield (26 mg, 0.04 mmol). ¹H NMR (400 MHz, CDCl₃): δ 8.44 (br s, 2H), 8.35 (d, J = 4.2 Hz, 2H), 8.28 (s, 1H), 7.60 (d, J = 8.0 Hz, 2H), 7.47(d, J = 8.2 Hz, 2H), 7.28 (m, 2H), 7.17 (s, 1H), 7.12 (d, J = 8.4 Hz, 2H), 3.89 (s, 3H), 1.90-1.88 (m, 4H), 1.21-1.14 (m, 12H), 0.96-0.93 (m, 4H), 0.82-0.79 (m, 6H). ¹³C {¹H} NMR (300 MHz, CDCl₃): δ 164.2, 158.4, 149.7, 147.2, 145.5, 144.9, 144.0, 143.1, 136.2, 134.7, 131.0, 127.2, 124.4, 117.2, 93.3, 65.9, 54.2, 53.0, 45.9, 37.7, 31.5, 29.7, 24.5, 22.6, 15.3, 14.05. IR (neat, cm⁻¹): 3032, 2923, 2851, 2207, 1713, 1567, 1479, 1411, 1248. HRMS ESI (positive mode) m/z calc'd for $C_{42}H_{44}N_4O_2S_2$ [M]⁺: 700.2906, found 700.2871.

Transient Absorption Spectroscopy. Film Fabrication. TAS films were fabricated as previously described. 60 The electrode was sensitized by immersing the ${\rm TiO_2}$ film into a 0.5 mM **DN1** solution of MeCN:t-BuOH (1:1) for 12 h.

Transient Absorption Measurements. Time-resolved absorption spectra were collected using an Edinburgh LP980 optical system. Excitation light of 532 nm (<2 mJ/pulse; 1 ns pulse) was provided by a Continuum Surelite pulsed Nd:YAG laser equipped with a doubling crystal, and the probe source was a 150 W pulsed xenon arc lamp. TiO_2 electrodes (3 μ m thick) were used for the transient absorption measurements. The devices were positioned at a 45° angle relative to the pump and probe sources in order to maximize overlap and direct scattered light away from the entrance slit to the monochromator.

DSC Device Fabrication and Characterization. Devices were prepared and characterized with equipment as previously described. The electrode was sensitized by immersing the TiO₂ film into a 0.5 mM DN1 solution of MeCN:*t*-BuOH (1:1) for 12 h. PEDOT counter electrodes were used for all DSC devices and were made according to literature procedure. ⁶²

ASSOCIATED CONTENT

Supporting Information

The Supporting Information is available free of charge at https://pubs.acs.org/doi/10.1021/acsaem.1c02912.

Additional DSC device characterization, transient absorption studies, NMR data, and electrochemical analysis results (PDF)

AUTHOR INFORMATION

Corresponding Authors

Jared H. Delcamp — Department of Chemistry and Biochemistry, University of Mississippi, University, Mississippi 38677, United States; Orcid.org/0000-0001-5313-4078; Email: delcamp@olemiss.edu

Nathan I. Hammer — Department of Chemistry and Biochemistry, University of Mississippi, University, Mississippi 38677, United States; orcid.org/0000-0002-6221-2709; Email: nhammer@olemiss.edu

Jonah W. Jurss – Department of Chemistry and Biochemistry, University of Mississippi, University, Mississippi 38677, *United States;* orcid.org/0000-0002-2780-3415; Email: jwjurss@olemiss.edu

Authors

Dinesh Nugegoda — Department of Chemistry and Biochemistry, University of Mississippi, University, Mississippi 38677, United States; Occid.org/0000-0002-5456-8940

Leigh Anna Hunt — Department of Chemistry and Biochemistry, University of Mississippi, University, Mississippi 38677, United States; Occid.org/0000-0002-7681-3599

Anthony Devdass — Department of Chemistry and Biochemistry, University of Mississippi, University, Mississippi 38677, United States; orcid.org/0000-0002-0279-1585

Hammad Cheema – Department of Chemistry and Biochemistry, University of Mississippi, University, Mississippi 38677, United States; orcid.org/0000-0002-7045-0141

Ryan C. Fortenberry – Department of Chemistry and Biochemistry, University of Mississippi, University, Mississippi 38677, United States; orcid.org/0000-0003-4716-8225

Complete contact information is available at: https://pubs.acs.org/10.1021/acsaem.1c02912

Author Contributions

[†]D.N. and L.A.H. contributed equally.

Author Contributions

The manuscript was written through contributions of all authors. All authors have given approval to the final version of the manuscript.

Funding

NSF award OIA-1757220 provided funding for the dye and RS synthesis and characterization as well as the DSC device fabrication and testing. The TAS studies were supported by NSF award 1954922.

Notes

The authors declare no competing financial interest.

REFERENCES

- (1) Cheema, H.; Watson, J.; Delcamp, J. H. Integrating GaAs, Si, and Dye-Sensitized Solar Cells in Multijunction Devices and Probing Harsh Condition Behavior. *ACS Appl. Electron. Mater.* **2021**, 3, 316–324.
- (2) Cao, Y.; Liu, Y.; Zakeeruddin, S. M.; Hagfeldt, A.; Grätzel, M. Direct Contact of Selective Charge Extraction Layers Enables High-Efficiency Molecular Photovoltaics. *Joule* **2018**, *2*, 1108–1117.
- (3) Freitag, M.; Teuscher, J.; Saygili, Y.; Zhang, X.; Giordano, F.; Liska, P.; Hua, J.; Zakeeruddin, S. M.; Moser, J.-E.; Grätzel, M.; Hagfeldt, A. Dye-sensitized solar cells for efficient power generation under ambient lighting. *Nat. Photon.* **2017**, *11*, 372–378.
- (4) Zhang, D.; Stojanovic, M.; Ren, Y.; Cao, Y.; Eickemeyer, F. T.; Socie, E.; Vlachopoulos, N.; Moser, J. E.; Zakeeruddin, S. M.; Hagfeldt, A.; Gratzel, M. A molecular photosensitizer achieves a Voc of 1.24 V enabling highly efficient and stable dye-sensitized solar cells with copper(II/I)-based electrolyte. *Nat. Commun.* **2021**, *12*, 1777.
- (5) Munoz-Garcia, A. B.; Benesperi, I.; Boschloo, G.; Concepcion, J. J.; Delcamp, J. H.; Gibson, E. A.; Meyer, G. J.; Pavone, M.; Pettersson, H.; Hagfeldt, A.; Freitag, M. Dye-sensitized solar cells strike back. *Chem. Soc. Rev.* **2021**, *50*, 12450–12550.
- (6) Yoon, S.; Tak, S.; Kim, J.; Jun, Y.; Kang, K.; Park, J. Application of transparent dye-sensitized solar cells to building integrated photovoltaic systems. *Build. Environ.* **2011**, *46*, 1899–1904.

- (7) Jelle, B. P.; Breivik, C. The Path to the Building Integrated Photovoltaics of Tomorrow. *Energy Procedia* **2012**, *20*, 78–87.
- (8) Biyik, E.; Araz, M.; Hepbasli, A.; Shahrestani, M.; Yao, R.; Shao, L.; Essah, E.; Oliveira, A. C.; del Caño, T.; Rico, E.; Lechón, J. L.; Andrade, L.; Mendes, A.; Atlı, Y. B. A key review of building integrated photovoltaic (BIPV) systems. *Eng. Sci. Technol.* **2017**, 20, 833–858.
- (9) Saifullah, M.; Gwak, J.; Yun, J. H. Comprehensive review on material requirements, present status, and future prospects for building-integrated semitransparent photovoltaics (BISTPV). *J. Mater. Chem. A* **2016**, *4*, 8512–8540.
- (10) Roy, A.; Ghosh, A.; Bhandari, S.; Selvaraj, P.; Sundaram, S.; Mallick, T. K. Color Comfort Evaluation of Dye-Sensitized Solar Cell (DSSC) Based Building-Integrated Photovoltaic (BIPV) Glazing after 2 Years of Ambient Exposure. *J. Phys. Chem. C* **2019**, *123*, 23834–23837.
- (11) Tsao, H. N.; Gratzel, M. Illumination Time Dependent Learning in Dye Sensitized Solar Cells. *ACS Appl. Mater. Interfaces* **2018**, *10*, 36602–36607.
- (12) Michaels, H.; Rinderle, M.; Freitag, R.; Benesperi, I.; Edvinsson, T.; Socher, R.; Gagliardi, A.; Freitag, M. Dye-sensitized solar cells under ambient light powering machine learning: towards autonomous smart sensors for the internet of things. *Chem. Sci.* **2020**, *11*, 2895—2906.
- (13) Aslam, A.; Mehmood, U.; Arshad, M. H.; Ishfaq, A.; Zaheer, J.; Ul Haq Khan, A.; Sufyan, M. Dye-sensitized solar cells (DSSCs) as a potential photovoltaic technology for the self-powered internet of things (IoTs) applications. *Solar Energy* **2020**, 207, 874–892.
- (14) Hagfeldt, A.; Boschloo, G.; Sun, L.; Kloo, L.; Pettersson, H. Dye-Sensitized Solar Cells. *Chem. Rev.* **2010**, *110*, 6595–6663.
- (15) Sun, Z.; Liang, M.; Chen, J. Kinetics of Iodine-Free Redox Shuttles in Dye-Sensitized Solar Cells: Interfacial Recombination and Dye Regeneration. *Acc. Chem. Res.* **2015**, *48*, 1541–1550.
- (16) Jeon, J.; Park, Y. C.; Han, S. S.; Goddard, W. A., 3rd; Lee, Y. S.; Kim, H. Rapid Dye Regeneration Mechanism of Dye-Sensitized Solar Cells. *J. Phys. Chem. Lett.* **2014**, *5*, 4285–4290.
- (17) Simon, S. J. C.; Parlane, F. G. L.; Swords, W. B.; Kellett, C. W.; Du, C.; Lam, B.; Dean, R. K.; Hu, K.; Meyer, G. J.; Berlinguette, C. P. Halogen Bonding Promotes Higher Dye-Sensitized Solar Cell Photovoltages. *J. Am. Chem. Soc.* **2016**, *138*, 10406–10409.
- (18) Swords, W. B.; Simon, S. J.; Parlane, F. G.; Dean, R. K.; Kellett, C. W.; Hu, K.; Meyer, G. J.; Berlinguette, C. P. Evidence for Interfacial Halogen Bonding. *Angew. Chem., Int. Ed.* **2016**, *55*, 5956–5960.
- (19) Parlane, F. G. L.; Mustoe, C.; Kellett, C. W.; Simon, S. J.; Swords, W. B.; Meyer, G. J.; Kennepohl, P.; Berlinguette, C. P. Spectroscopic detection of halogen bonding resolves dye regeneration in the dye-sensitized solar cell. *Nat. Commun.* **2017**, *8*, 1761.
- (20) Chen, D. Y.; Hsu, Y. Y.; Hsu, H. C.; Chen, B. S.; Lee, Y. T.; Fu, H.; Chung, M. W.; Liu, S. H.; Chen, H. C.; Chi, Y.; Chou, P. T. Organic dyes with remarkably high absorptivity; all solid-state dye sensitized solar cell and role of fluorine substitution. *Chem. Commun.* **2010**, *46*, 5256–5258.
- (21) Tsao, H. N.; Yi, C.; Moehl, T.; Yum, J. H.; Zakeeruddin, S. M.; Nazeeruddin, M. K.; Grätzel, M. Cyclopentadithiophene bridged donor-acceptor dyes achieve high power conversion efficiencies in dye-sensitized solar cells based on the tris-cobalt bipyridine redox couple. *ChemSusChem* **2011**, *4*, 591–594.
- (22) Ahmad, S.; Bessho, T.; Kessler, F.; Baranoff, E.; Frey, J.; Yi, C.; Gratzel, M.; Nazeeruddin, M. K. A new generation of platinum and iodine free efficient dye-sensitized solar cells. *Phys. Chem. Chem. Phys.* **2012**, *14*, 10631–10639.
- (23) Cao, Y.; Saygili, Y.; Ummadisingu, A.; Teuscher, J.; Luo, J.; Pellet, N.; Giordano, F.; Zakeeruddin, S. M.; Moser, J. E.; Freitag, M.; Hagfeldt, A.; Gratzel, M. 11% efficiency solid-state dye-sensitized solar cells with copper(II/I) hole transport materials. *Nat. Commun.* 2017, 8, 15390.
- (24) Gabrielsson, E.; Ellis, H.; Feldt, S.; Tian, H.; Boschloo, G.; Hagfeldt, A.; Sun, L. Convergent/Divergent Synthesis of a Linker-

- Varied Series of Dyes for Dye-Sensitized Solar Cells Based on the D35 Donor. *Adv. Energy Mater.* **2013**, *3*, 1647–1656.
- (25) Zhang, L.; Cole, J. M. Anchoring groups for dye-sensitized solar cells. ACS Appl. Mater. Interfaces 2015, 7, 3427–3455.
- (26) Kashif, M. K.; Axelson, J. C.; Duffy, N. W.; Forsyth, C. M.; Chang, C. J.; Long, J. R.; Spiccia, L.; Bach, U. A new direction in dyesensitized solar cells redox mediator development: in situ fine-tuning of the cobalt(II)/(III) redox potential through Lewis base interactions. J. Am. Chem. Soc. 2012, 134, 16646–16653.
- (27) Topchiy, M. A.; Dzhevakov, P. B.; Rubina, M. S.; Morozov, O. S.; Asachenko, A. F.; Nechaev, M. S. Solvent-Free Buchwald-Hartwig (Hetero)arylation of Anilines, Diarylamines, and Dialkylamines Mediated by Expanded-Ring N-Heterocyclic Carbene Palladium Complexes. Eur. J. Org. Chem. 2016, 2016, 1908—1914.
- (28) Karsten, B. P.; Bijleveld, J. C.; Viani, L.; Cornil, J.; Gierschner, J.; Janssen, R. A. J. Electronic structure of small band gap oligomers based on cyclopentadithiophenes and acceptor units. *J. Mater. Chem.* **2009**, *19*, 5343–5350.
- (29) Huang, Z. S.; Zang, X. F.; Hua, T.; Wang, L.; Meier, H.; Cao, D. 2,3-Dipentyldithieno[3,2-f:2',3'-h]quinoxaline-Based Organic Dyes for Efficient Dye-Sensitized Solar Cells: Effect of pi-Bridges and Electron Donors on Solar Cell Performance. ACS Appl. Mater. Interfaces 2015, 7, 20418–20429.
- (30) Wallace, A. M.; Curiac, C.; Delcamp, J. H.; Fortenberry, R. C. Accurate determination of the onset wavelength (λ_{onset}) in optical spectroscopy. *J. Quant. Spectrosc. Radiat. Transf.* **2021**, 265, 107544.
- (31) Urbani, M.; Grätzel, M.; Nazeeruddin, M. K.; Torres, T. Meso-Substituted Porphyrins for Dye-Sensitized Solar Cells. *Chem. Rev.* **2014**, *114*, 12330–12396.
- (32) Anderson, A. Y.; Barnes, P. R. F.; Durrant, J. R.; O'Regan, B. C. Quantifying Regeneration in Dye-Sensitized Solar Cells. *J. Phys. Chem.* C **2011**, *115*, 2439–2447.
- (33) Boschloo, G.; Häggman, L.; Hagfeldt, A. Quantification of the Effect of 4-tert-Butylpyridine Addition to I^-/I_3^- Redox Electrolytes in Dye-Sensitized Nanostructured TiO_2 Solar Cells. *J. Phys. Chem. B* **2006**, *110*, 13144–13150.
- (34) Long, H.; Zhou, D.; Zhang, M.; Peng, C.; Uchida, S.; Wang, P. Probing Dye-Correlated Interplay of Energetics and Kinetics in Mesoscopic Titania Solar Cells with 4-tert-Butylpyridine. *J. Phys. Chem. C* 2011, *115*, 14408–14414.
- (35) Polander, L. E.; Yella, A.; Teuscher, J.; Humphry-Baker, R.; Curchod, B. F. E.; Ashari Astani, N.; Gao, P.; Moser, J.-E.; Tavernelli, I.; Rothlisberger, U.; Grätzel, M.; Nazeeruddin, M. K.; Frey, J. Unravelling the Potential for Dithienopyrrole Sensitizers in Dye-Sensitized Solar Cells. *Chem. Mater.* **2013**, *25*, 2642–2648.
- (36) Lindsey, C. P.; Patterson, G. D. Detailed comparison of the Williams-Watts and Cole-Davidson functions. *J. Chem. Phys.* **1980**, 73, 3348-3357.
- (37) Lukichev, A. Physical meaning of the stretched exponential Kohlrausch function. *Phys. Lett. A* **2019**, 383, 2983–2987.
- (38) Kohlrausch, R. Theorie des elektrischen Rückstandes in der Leidener Flasche. *Ann. Phys. (Pogg.)* **1854**, *167*, 179–214.
- (39) Williams, G.; Watts, D. C. Non-Symmetrical Dielectric Relaxation Behaviour Arising from a Simple Empirical Decay Function. *Trans. Faraday Soc.* **1970**, *66*, 80–85.
- (40) Casarin, L.; Swords, W. B.; Caramori, S.; Bignozzi, C. A.; Meyer, G. J. Rapid Static Sensitizer Regeneration Enabled by Ion Pairing. *Inorg. Chem.* **2017**, *56*, 7324–7327.
- (41) DiMarco, B. N.; Troian-Gautier, L.; Sampaio, R. N.; Meyer, G. J. Dye-sensitized electron transfer from TiO2 to oxidized triphenylamines that follows first-order kinetics. *Chem. Sci.* **2018**, *9*, 940–949.
- (42) Peddapuram, A.; Cheema, H.; Adams, R. E.; Schmehl, R. H.; Delcamp, J. H. A Stable Panchromatic Green Dual Acceptor, Dual Donor Organic Dye for Dye-Sensitized Solar Cells. *J. Phys. Chem. C* **2017**, *121*, 8770–8780.
- (43) Cheema, H.; Peddapuram, A.; Adams, R. E.; McNamara, L. E.; Hunt, L. A.; Le, N.; Watkins, D. L.; Hammer, N. I.; Schmehl, R. H.; Delcamp, J. H. Molecular Engineering of NIR Absorbing Thienopyr-

- azine Double Donor Double Acceptor Organic Dyes for DSCs. J. Org. Chem. 2017, 82, 12038–12049.
- (44) King, A. E.; Surendranath, Y.; Piro, N. A.; Bigi, J. P.; Long, J. R.; Chang, C. J. A mechanistic study of proton reduction catalyzed by a pentapyridine cobalt complex: evidence for involvement of an anation-based pathway. *Chem. Sci.* **2013**, *4*, 1578–1587.
- (45) Li, F.; Jennings, J. R.; Wang, Q. Determination of sensitizer regeneration efficiency in dye-sensitized solar cells. *ACS Nano* **2013**, 7, 8233–8242.
- (46) Cho, I.; Wagner, P.; Innis, P. C.; Mori, S.; Mozer, A. J. Substrate-Dependent Electron-Transfer Rate of Mixed-Ligand Electrolytes: Tuning Electron-Transfer Rate without Changing Driving Force. J. Am. Chem. Soc. 2021, 143, 488–495.
- (47) Yang, J.; Ganesan, P.; Teuscher, J.; Moehl, T.; Kim, Y. J.; Yi, C.; Comte, P.; Pei, K.; Holcombe, T. W.; Nazeeruddin, M. K.; Hua, J.; Zakeeruddin, S. M.; Tian, H.; Grätzel, M. Influence of the Donor Size in D-pi-A Organic Dyes for Dye-Sensitized Solar Cells. *J. Am. Chem. Soc.* **2014**, *136*, 5722–5730.
- (48) Freitag, M.; Giordano, F.; Yang, W.; Pazoki, M.; Hao, Y.; Zietz, B.; Grätzel, M.; Hagfeldt, A.; Boschloo, G. Copper Phenanthroline as a Fast and High-Performance Redox Mediator for Dye-Sensitized Solar Cells. *J. Phys. Chem. C* **2016**, *120*, 9595–9603.
- (49) Gehlen, M. H. The centenary of the Stern-Volmer equation of fluorescence quenching: From the single line plot to the SV quenching map. J. Photochem. Photobio. C: Photochem. Rev. 2020, 42, 100338.
- (50) Yang, W.; Chen, X.; Su, H.; Fang, W.; Zhang, Y. The fluorescence regulation mechanism of the paramagnetic metal in a biological HNO sensor. *Chem. Commun.* **2015**, *51*, 9616–9619.
- (51) Chai, J. D.; Head-Gordon, M. Long-range corrected hybrid density functionals with damped atom-atom dispersion corrections. *Phys. Chem. Phys.* **2008**, *10*, 6615–6620.
- (52) Francl, M. M.; Pietro, W. J.; Hehre, W. J.; Binkley, J. S.; Gordon, M. S.; DeFrees, D. J.; Pople, J. A. Self-consistent molecular orbital methods. XXIII. A polarization-type basis set for second-row elements. *J. Chem. Phys.* **1982**, *77*, 3654–3665.
- (53) Hehre, W. J.; Ditchfield, R.; Pople, J. A. Self—Consistent Molecular Orbital Methods. XII. Further Extensions of Gaussian—Type Basis Sets for Use in Molecular Orbital Studies of Organic Molecules. *J. Chem. Phys.* **1972**, *56*, 2257–2261.
- (54) Feller, D. The Role of Databases in Support of Computational Chemistry Calculations. *J. Comput. Chem.* **1996**, *17*, 1571–1586.
- (55) Sun, Y.; Bigi, J. P.; Piro, N. A.; Tang, M. L.; Long, J. R.; Chang, C. J. Molecular cobalt pentapyridine catalysts for generating hydrogen from water. *J. Am. Chem. Soc.* **2011**, *133*, 9212–9215.
- (56) Zhang, W.; Wu, Y.; Bahng, H. W.; Cao, Y.; Yi, C.; Saygili, Y.; Luo, J.; Liu, Y.; Kavan, L.; Moser, J.-E.; Hagfeldt, A.; Tian, H.; Zakeeruddin, S. M.; Zhu, W.-H.; Grätzel, M. Comprehensive control of voltage loss enables 11.7% efficient solid-state dye-sensitized solar cells. *Energy Environ. Sci.* 2018, 11, 1779—1787.
- (57) Garcia-Rodriguez, R.; Jiang, R.; Canto-Aguilar, E. J.; Oskam, G.; Boschloo, G. Improving the mass transport of copper-complex redox mediators in dye-sensitized solar cells by reducing the interelectrode distance. *Phys. Chem. Chem. Phys.* **2017**, *19*, 32132–32142.
- (58) Feldt, S. M.; Gibson, E. A.; Gabrielsson, E.; Sun, L.; Boschloo, G.; Hagfeldt, A. Design of Organic Dyes and Cobalt Polypyridine Redox Mediators for High-Efficiency Dye-Sensitized Solar Cells. *J. Am. Chem. Soc.* **2010**, *132*, 16714–16724.
- (59) Frisch, M. J.; Trucks, G. W.; Schlegel, H. B.; Scuseria, G. E.; Robb, M. A.; Cheeseman, J. R.; Scalmani, G.; Barone, V.; Petersson, G. A.; Nakatsuji, H.; Li, X.; Caricato, M.; Marenich, A. V.; Blolino, J.; Janesko, B. G.; Gomperts, R.; Mennucci, B.; Hratchian, H. P.; Ortiz, J. V.; Izmaylov, A. F.; Sonnenberg, J. L.; Williams-Young, D.; Ding, F.; Lipparini, F.; Egidi, F.; Goings, J.; Peng, B.; Petrone, A.; Henderson, T.; Ranasinghe, D.; Zakrzewski, V. G.; Gao, J.; Rega, N.; Zheng, G.; Liang, W.; Hada, M.; Ehara, M.; Toyota, K.; Fukuda, R.; Hasegawa, J.; Ishida, M.; Nakajima, T.; Honda, Y.; Kitao, O.; Nakai, H.; Vreven, T.; Throssell, K.; Montgomery, J. A., Jr.; Peralta, J. E.; Oligaro, F.; Bearpark, M. J.; Heyd, J. J; Brothers, E. N.; Kudin, K. N.; Staroverov,

- V. N.; Keith, T. A.; Kobayashi, R.; Normand, J.; Ragavachari, K.; Rendell, A. P.; Burant, J. C.; Iyengar, S. S.; Tomasi, J.; Cossi, M.; Millam, J. M.; Klene, M.; Adamo, C.; Cammi, R.; Ochterski, J. W.; Martin, R. L.; Morokuma, K.; Farkas, O.; Foresman, J. B.; Fox, D. J. *Gaussian 16*, revision A.03; Gaussian, Inc.: Wallingford, CT, 2016.
- (60) Curiac, C.; Hunt, L. A.; Sabuj, M. A.; Li, Q.; Baumann, A.; Cheema, H.; Zhang, Y.; Rai, N.; Hammer, N. I.; Delcamp, J. H. Probing Interfacial Halogen-Bonding Effects with Halogenated Organic Dyes and a Lewis Base-Decorated Transition Metal-Based Redox Shuttle at a Metal Oxide Interface in Dye-Sensitized Solar Cells. J. Phys. Chem. C 2021, 125, 17647–17659.
- (61) Rodrigues, R. R.; Lee, J. M.; Taylor, N. S.; Cheema, H.; Chen, L.; Fortenberry, R. C.; Delcamp, J. H.; Jurss, J. W. Copper-based redox shuttles supported by preorganized tetradentate ligands for dyesensitized solar cells. *Dalton Trans.* **2020**, *49*, 343–355.
- (62) Ellis, H.; Vlachopoulos, N.; Häggman, L.; Perruchot, C.; Jouini, M.; Boschloo, G.; Hagfeldt, A. PEDOT counter electrodes for dyesensitized solar cells prepared by aqueous micellar electrodeposition. *Electrochim. Acta* **2013**, *107*, 45–51.